International Journal of Applied Mechanics
Vol. 5, No. 3 (2013) 1350024 (17 pages)

DOI: 10.1142/S1758825113500245

Imperial College Press
www.icpress.co.uk

BREAKING ANALYSIS OF ARTIFICIAL ELASTIC TUBES AND HUMAN ARTERY

W. G. LI*, J. GOING†, N. A. HILL*
and X. Y. LUO*,‡

*School of Mathematics & Statistics
University of Glasgow, Glasgow
G12 8QW, UK

†Institute of Cancer Sciences, University of Glasgow
Glasgow, UK
‡xiaoyu.luo@glasgow.ac.uk

Received 7 February 2013
Revised 23 May 2013
Accepted 24 May 2013
Published 6 September 2013

Mechanical behaviors of artificial elastic tubes are studied to see if the fibre orientation in these vessels is optimal by comparison with those of human artery. By optimal we mean that the strengths of stretching and inflation in the vessels are equally good. Artificial thin film tubes have many applications in the food and fruit packing industry. In this paper, the wall of thin-film elastic tubes is considered as a fibre-reinforced membrane with two families of fibres and a uniform matrix material. Their mechanical properties are determined using a structure-based constitutive law. The constitutive parameters are inversely estimated from two separate uniaxial tensile tests in the circumferential and longitudinal directions. The inflation model for the elastic tubes and human common carotid artery are developed to investigate their breaking characteristics, and to explore the optimal fibre orientations. Results show that the fibre orientation has an important effect on the break behavior of the elastic tubes, and the tubes investigated are much weaker in the circumferential direction. On the other hand, the fibre orientation is close to the optimal state in the human common carotid artery.

Keywords: Nonlinear mechanics; finite strain; anisotropy; fibre reinforced material; thin-film; artificial tubes; elastic tube; artery; constitutive law; damage; break; inverse method.

1. Introduction

Artificial films and coatings have found use in a variety of applications, e.g., sausage skins, chocolate casings, and wax coating for fruits and vegetables. It is important to study these artificial tubes from mechanics point of view, as the films must have sufficient strength to prevent damage during packing and transportation. Indeed, various experimental studies have been carried out, and the methods of mechanical tests of the artificial films, including tensile modulus, yielding stress and strain, breaking stress and strain, and the Charpy impact strength, have now been specified

in Standards ISO 527-1,-2 and ISO179/1eU. In particular, methods for conducting tensile strength measurement on bioplolymer films have been proposed [Stevens and Poliks, 2003].

These artificial films used in food industry normally exhibit highly nonlinear stress–strain behavior during simple tensile tests because they are made of animal collagen and various polymers, and other minor constituents. The tubes of the artificial film are often manufactured by extrusion and blow-molding methods with rotary extruders, so that the strengthening fibres are aligned with preferred orientations.

In this paper, we question if current designs of artificial tubes are optimal under axial stretching and internal pressure. In this context, we also study the mechanical behavior of human artery with similar material structure and subject to similar loading conditions. This allows us to compare the mechanical performance of these two types of "fibre reinforced tubes." We start by reviewing the current literature on damage studies of human arteries.

The artery wall is incompressible, nonlinear and inhomogeneous. It exhibits hysteresis under a cyclic loading and its fibrous structure, i.e., the collagen and elastin fibres, can be torn when subject to higher than the physiological pressure [Chu *et al.* 1972; Hokanson and Yazdani, 1997]. This often first appears as a microtearing that could contribute to a larger scale damage [Hokanson and Yazdani, 1997]. Like a rubber material, damage to the arterial wall is closely related to the maximum strain [Hokanson and Yazdani, 1997]. Under steady loading, the artery cannot be damaged until the maximum strain is achieved. Under cyclic loading the loading and unloading stress–strain path of the artery is the same until the maximum strain is exceeded [Hokanson and Yazdani, 1997]. Such behavior is called the Mullin or softening effect, which was originally used to describe the behavior of rubber [Diani *et al.*, 2009]. In rubbers, once the maximum von Mises stress or strain exceeds a critical value, the material is deemed to have failed [Volokh, 2008]. However, such local failure does not lead to the total failure of the soft tissue in the artery. Hence, the traditional methods of predicting failure of rubber material may not be suitable for artery. New methods for predicting the total or global failure of arterial wall are required to describe the degraded state of the soft tissue structure of human artery.

In recent years, concepts from damage mechanics have increasingly been applied to the damage prediction for soft tissue. Damage mechanics is the study of the initiation, propagation and fracture of materials using state variables that represent the effects of damage on the stiffness and the remaining life of a material subject to thermal, mechanical loading, or ageing. The state variables may be measurable variables or material parameters.

Hokanson and Yazdani [1997] used an Ogden strain energy function for arteries and proposed an exponential damage function using the equivalent strain of collagen fibres as the material damage criterion. However, the softening is not explicitly included in the model. In Volokh [2008] the chosen damage criteria are the matrix

material strength and two indices for the softening effect. They used the two-layer artery model of Holzapfel *et al.* [2000], and showed that the failure of adventitia occurs first but the artery does not fail until the fibres fail.

For cerebral arterial tissue, the elastin damage effect was studied by Li and Robertson [2009] using the strain energy approach by Gasser *et al.* [2006] for elastin and collagen fibres. The Cauchy stress is estimated from material properties experimentally determined; and the stress generated by the elastin is corrected by three scaled damage variables that indicate strain-based damage (cyclic stretch or fatigue) and enzymatic damage due to haemodynamic wall shear stress. An exponential damage function was used. However, the fibre damage was not addressed by this group.

In contrast to Li and Robertson [2009], Balzani *et al.* [2012] proposed that the main damage should occur in the fibres of the arterial walls because the fibres bear the major cycling loads. Therefore, they introduced a new damage state variable, which is an exponential function of the difference in the strain energy function between the current and reference configurations. Similar work was carried out by Calvo *et al.* [2009], Marini *et al.* [2012], Martins *et al.* [2012] for various bio-soft tissues.

A combined matrix and fibre strain-driven damage model is proposed by Alastrué *et al.* [2007], where a damage state variable is correlated to a parabolic damage function that itself is a function of strain energy. They also accounted for the softening effects in the matrix and fibres, and provided better agreement with experimental data than the previous models.

In this paper, we consider a much simpler macroscopic "damage" model of artery and thin film tubes, and assume that these models can be damaged by breaking when the internal pressure and axial force reach a critical loading condition. This work is motivated by the observation that the artificial tubes resemble the structure of human arteries, and hence can be modeled using a homogeneous matrix and two families of fibres [Holzapfel *et al.*, 2005a]. To identify the constitutive parameters, we make use of uniaxial tensile tests for specimens taken from the artificial tubes in the circumferential and longitudinal directions. We then develop two tube models with these constitutive parameters and run simulations to model the tube behavior near breaking. The results are compared with that of human common carotid artery [Sommer, 2008], and differences are discussed.

Finally, we examine the effects of fibre angle on the tube deformation and explore the optimal fibre orientations when the circumferential and longitudinal breaks occur simultaneously.

2. Methods and Models

2.1. *Tensile tests*

To provide useful information about the quality of elastic tubes, tensile strength tests are carried out in the laboratory. In those tests two dog-bone-shaped specimens

are cut off from an artificial tube of diameter $d = 28\,\text{mm}$ in the circumferential and longitudinal direction by using a template which allows a specimen to have $W_0 = 38\,\text{mm}$ length and $H_0 = 13\,\text{mm}$ height (see Fig. 1). The specimens are then clamped in place and stretched on a computer-aided simple tensile strength measuring device until they are broken. The loading–strain curves in both the directions are recorded, resulting into a typical diagram shown in Fig. 1(c), where the material clearly exhibits an anisotropic and nonlinear behavior with greater stiffness in the longitudinal direction and different break strengths in the both directions.

Since the tube was extruded by using a coaxial contra-rotating extruder, the gel in the gap between two mandrels was subject to three motions: two contra-shearing motions near the solid boundaries of the gap and an axial flow in the gap along the axial direction of the tube. This suggests the two families of fibres, which may not be continuously distributed, can be embedded in the wall of the tube with uniform thickness.

We postulated that the tube wall with a thickness of 0.0203 mm is a single layer wall composed of two families of fibres and a homogeneous matrix material [Fig. 2(a)], and that it can be described by the constitutive model developed for arteries [Holzapfel *et al.*, 2000; Holzapfel *et al.*, 2005a]. The constitutive parameters are estimated using the tensile test data as shown in Fig. 1(c).

From the tube, shown in Fig. 2(a), two specimens are cut in the longitudinal (L) and the circumferential (C) directions, as are illustrated in Figs. 2(b) and 2(c). For the specimen in Fig. 2(b), the longitudinal loading is applied in the simple tensile test, thus only the longitudinal normal stress exists which is uniform across the circumferential direction (σ_L = constant). Along the thickness direction we have

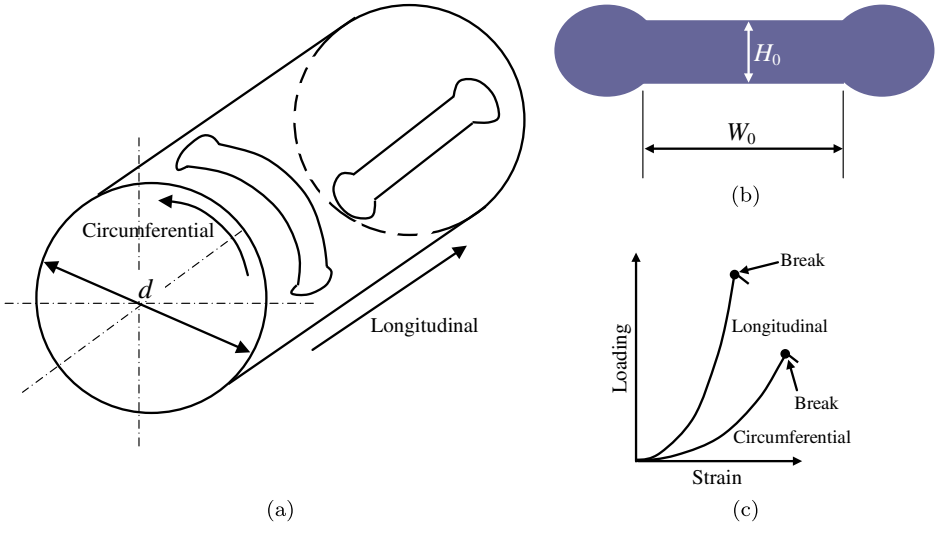

Fig. 1. A tube of artificial elastic film (a), a dog-bone-shaped specimen cut from tube body (b) and typical loading–strain curves (c).

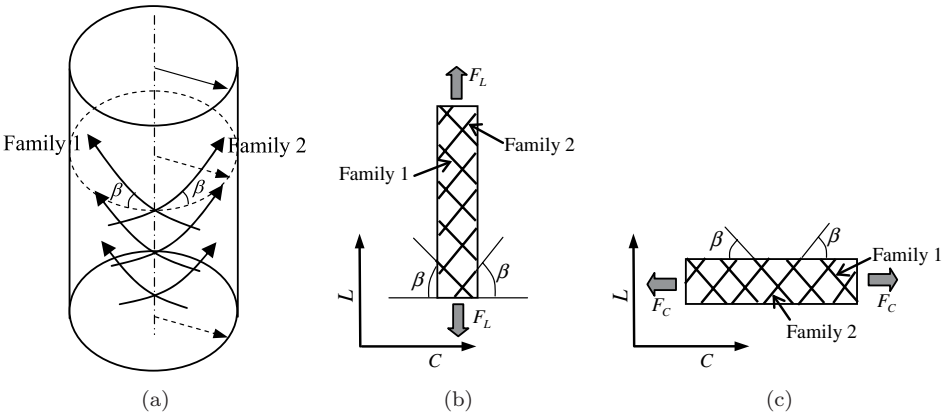

(a) (b) (c)

Fig. 2. The tube casing consists of two families of fibres and homogenous matrix material, a specimen is cut in the longitudinal (L) direction and one is taken in the circumferential (C) direction, (a) tube, (b) specimen in the longitude direction, (c) specimen in the circumferential direction.

zero circumferential stress ($\sigma_c = 0$) [Beer and Johnston, 1981]. Similarly, for the specimen in Fig. 2(c), we have $\sigma_L = 0$, and $\sigma_c = \text{const}$, respectively.

2.2. *Microscopic observations*

To compare with the model predictions, the thin film tubes were photographed using a $\times 10$ flat-field objective on an Olympus BX51 light microscope, between crossed polarizing filters. This showed birefringent fibres against a dark background. The artificial tube samples were photographed when supported on standard 75×25 mm glass microscope slides, either in their natural dry state or following hydration in lukewarm water, flattening on the slide and being allowed to dry again. This reduced problems with the crinkled surface of the thin tubes. A stage micrometer with 10 micron divisions was photographed under the same conditions for scale calibration. Images were captured for intact tubes and of torn edges, as shown in Fig. 3. Although these images only directly show the cellulose orientations, these are believed to share the same orientation during the producing process.

2.3. *Mathematical models*

The strain energy function is taken as the same as proposed by Holzapfel *et al.* [2005a]

$$\psi = \mu(I_1 - 3) + \frac{k_1}{k_2}(\exp\{k_2[(1-\rho)(I_1-3)^2 + \rho(I_4-1)^2]\} - 1), \tag{1}$$

where μ and k_1 are, respectively, the stiffnesses of the matrix material and the two families of fibres, k_2 is the rate of the stiffness increase, ρ is the fibre anisotropy

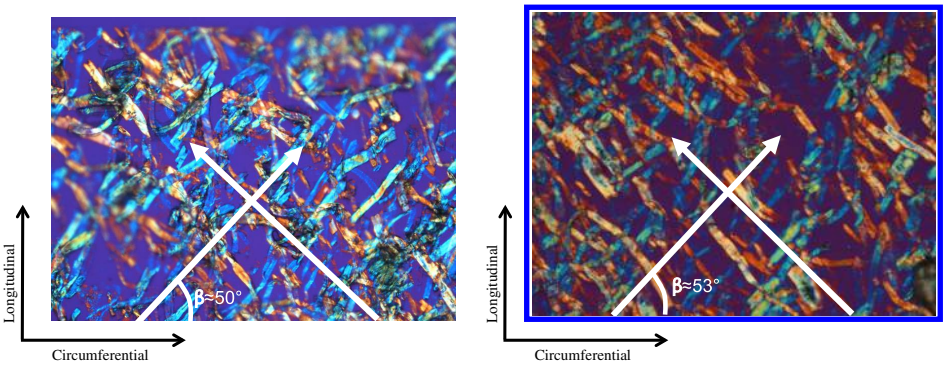

(a) (b)

Fig. 3. Observed cellulous orientations in the elastic tube walls under a microscope. These are believed to be the same as fibres orientations, and are strongly orientated in two main directions.

index: $\rho \in [0, 1], \rho = 0$ indicates that the material is isotropic, and $\rho = 1$ there is no fibre dispersion (Holzapfel *et al.*, 2005b). The invariants I_1 and I_4 are associated with the right Cauchy–Green tensor $\mathbf{C} = \mathbf{F}^{\mathbf{T}}\mathbf{F}$, $\mathbf{F}$ being the deformation gradient, and the orientations of two the families of fibres. If the fibre orientation is indicated by the unit vector $\mathbf{a}_0, \mathbf{a}_0 = \mathbf{i}_C \cos\beta + \mathbf{i}_L \sin\beta$, and $\mathbf{i}_C$ and $\mathbf{i}_L$ are the unit vectors in the circumferential and longitudinal directions, respectively, then

$$I_1 = \operatorname{tr} \mathbf{C}, \quad I_4 = \mathbf{a}_0 \cdot (\mathbf{C}\mathbf{a}_0). \tag{2}$$

In terms of the three stretch ratios in the circumferential, and longitudinal and thickness directions, they are

$$I_1 = \lambda_C^2 + \lambda_L^2 + \lambda_T^2, \quad I_4 = \lambda_C^2 \cos^2\beta + \lambda_L^2 \sin^2\beta, \tag{3}$$

were λ_C, λ_L and λ_T are the stretch ratios in the circumferential, longitudinal and thickness directions, defined as $\lambda_C = W/W_0, \lambda_L = H/H_0$ and $\lambda_T = T/T_0$, respectively. These are related by the incompressibility condition $\lambda_C\lambda_L\lambda_T = 1$. T and T_0 are the loaded thickness of the specimen and stress-free thickness, respectively. Since the thickness of the casing is small, we assume it remains unchanged during the simple tensile test, i.e., $\lambda_T = 1$. With this assumption and the fact that λ_L is known during the simple tensile test, Eq. (2) can be simplified to

$$I_1 = \lambda_C^2 + \lambda_L^2 + \lambda_C^{-1}\lambda_L^{-1}, \quad I_4 = \lambda_C^2 \cos^2\beta + \lambda_L^2 \sin^2\beta. \tag{3}$$

For the first tensile test, the loading is only applied along the longitudinal direction, so the stress components are

$$\begin{cases} \sigma_L = 2(\lambda_L^2 - 1)\dfrac{\partial\psi}{\partial I_1} + 2\lambda_L^2 \sin^2\beta \dfrac{\partial\psi}{\partial I_4} \\ \sigma_C = 0 \end{cases} \tag{4}$$

Clearly, the longitudinal stress depends on λ_L only, $\lambda_C = 1/\lambda_L$ in I_4 expression of Eq. (3).

For the second tensile test, the loading is applied along the circumferential direction only; the normal stress is the only nonzero stress component which is uniform across the longitudinal direction and the thickness direction. Hence, we have

$$\begin{cases} \sigma_L = 0 \\ \sigma_C = 2(\lambda_C^2 - 1)\dfrac{\partial \psi}{\partial I_1} + 2\lambda_C^2 \cos^2 \beta \dfrac{\partial \psi}{\partial I_4} \end{cases}, \tag{5}$$

where $\lambda_L = 1/\lambda_C$ in Eq. (3). Again the circumferential stress depends on λ_C only.

For the longitudinal tensile test [Fig. 2(b)], the Cauchy stress components are

$$\begin{cases} \sigma_{_L}^{\exp} = \lambda_L F_L / A_0 \\ \sigma_{_C}^{\exp} = 0 \end{cases}, \tag{6}$$

where A_0 is the cross-section of the specimen at stress-free state, $A_0 = H_0 T_0$; and F_L is the longitudinal loading. Similarly, for the circumferential test [Fig. 2(c)], the Cauchy stress components are

$$\begin{cases} \sigma_{_L}^{\exp} = 0 \\ \sigma_{_C}^{\exp} = \lambda_C F_C / A_0 \end{cases}, \tag{7}$$

where F_C is the circumferential loading.

To determine the five constants β, k_1, k_2, ρ and μ, we solve an optimization problem with the following objective (error) function

$$f(\mu, \beta, k_1, k_2, \rho) = \sum_{i=1}^{N_L} (\sigma_{L_i} - \sigma_{L_i}^{\exp})^2 + \sum_{j=1}^{N_C} (\sigma_{C_j} - \sigma_{C_j}^{\exp})^2, \tag{8}$$

where N_L, N_C are the total numbers of loadings in the tensile tests, and σ_{ij} and $\sigma_{ij}^{\exp}$ $(i = L, C)$ are the predicted and experimental Cauchy stress components. The Levenberg–Marquardt method [Marquardt, 1963] is used to solve Eq. (8) with a user developed MATLAB code, and the convergence is established when the variation of the objective function is below 10^{-6}.

2.4. *Breaking analysis*

With the material parameters determined, we now build a tube model for the breaking analysis. To simplify the analysis we use the circumferential strain $\varepsilon_{_C}^b$ and longitudinal strain $\varepsilon_{_L}^b$ to indicate the breaking strain, which are measured in the tensile tests mentioned in Sec. 2.1. The anisotropic tube model shown in Fig. 4 is subject to an internal pressure and an axial strain ε_L applied at the end of the tube. The tube has the radius $r_0 = 14\,\text{mm}$ and the length $z_0 = 100\,\text{mm}$ in the stress-free state.

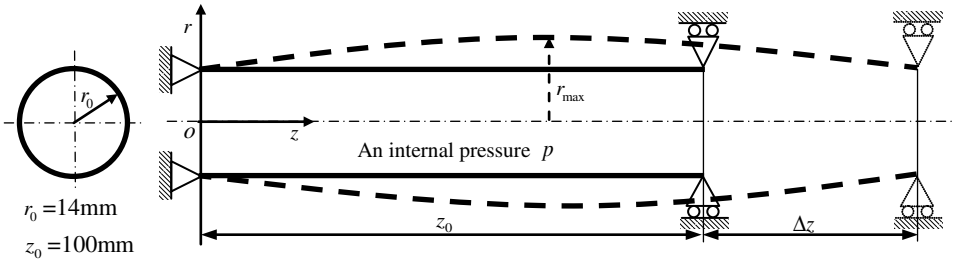

Fig. 4. Anisotropic tube model which is subject to internal pressure and axial force. The axial force is achieved by adding an axial displacement/strain in the z-direction.

Following Miehe [1994] and Wang *et al.* [2013], among others, we decompose the deformation gradient $\mathbf{F}$ into volumetric ($\mathbf{F}_{\rm vol}$) and isochoric ($\overline{\mathbf{F}}$) parts, i.e.,

$$\mathbf{F} = \bar{\mathbf{F}}\mathbf{F}_{\rm vol},\ \mathbf{F}_{\rm vol} = \mathrm{J}^{1/3}\mathbf{I},\ \bar{\mathbf{F}} = \mathrm{J}^{-1/3}\mathbf{F}, \tag{9}$$

where $\mathrm{J} = \det(\mathbf{F})$ and $\det(\bar{\mathbf{F}}) = 1$. The principle of virtual work is stated in the classical form as

$$\delta W_I = \int_{\rm V} \sigma : \delta\mathbf{D}\ \mathrm{dV} = \int_{\rm V_0} \mathrm{J}\sigma : \delta\mathbf{D}\ \mathrm{dV_0} = \int_{\rm S} \delta\mathbf{v}\cdot\mathbf{t}\ \mathrm{dS} + \int_{\rm V} \delta\mathbf{v}\cdot\mathbf{f}\ \mathrm{dV}, \tag{10}$$

in which V and $\mathrm{V_0}$ indicate volumes in the current and reference configurations, respectively, S is the surface of V, σ is the Cauchy stress tensor, $\delta\mathbf{D}$ is the virtual rate of deformation, $\mathbf{t}$ is the stress vector on the boundaries, $\mathbf{f}$ is the body force and it is zero here, and $\delta\mathbf{v}$ is the virtual displacement. The internal virtual work per unit volume in the reference configuration, δW_I, can be written as

$$\delta W_I = \int_{\rm V_0} \delta\psi\ \mathrm{dV_0} = \int_{\rm V_0} [\mathrm{J}((\sigma + q\mathbf{I}) : \delta\mathbf{e} - q\delta\varepsilon^{\rm vol}) - (\mathrm{J}-1)\delta q]\ \mathrm{dV_0}, \tag{11}$$

where $\delta\boldsymbol{\varepsilon}^{\mathbf{vol}} = \mathbf{I} : \delta\mathbf{D}$, is the virtual volumetric strain rate, $\mathbf{I}$ is the identity tensor, $\delta\mathbf{e} = \delta\mathbf{D} - \frac{1}{3}\delta\varepsilon^{\rm vol}\mathbf{I}$, is the virtual deviatoric strain rate, and $\delta\psi$ and δq are the variations of ψ and q, ψ is defined in Eq. (1), q is a Lagrange multiplier introduced to enforce the incompressibility constraint and is related to the Cauchy stress tensor by

$$\sigma = \mathbf{F}\sum_{i=1,4} \frac{\partial\psi}{\partial I_i}\frac{\partial I_i}{\partial\mathbf{F}} - q\mathbf{I}. \tag{12}$$

When the tube breaks, one of following criteria must be satisfied:

$$\begin{cases} \varepsilon_{c\,\max} = \varepsilon_c^b \\ \varepsilon_{L\,\max} = \varepsilon_L^b \end{cases}. \tag{13}$$

We solve the problem using the finite element package ABAQUS and user-subroutines; the internal pressure p and the longitudinal strain ε_L are incremented between pressure, $p \in [0, p_{\max}]$, where $p_{\max}$ is the maximum pressure applied.

The pressure loading profile is determined from the experimental $\sigma_L - \varepsilon_L$ relations of the tubes normalized by the maximum $\sigma_{L\,\max}$ and $\varepsilon_{L\,\max}$. The axial loading

(stretching) is increased linearly with $\varepsilon_L/\varepsilon_{L\max}$. Details are shown in Table 1 for the elastic tubes. The measured loading profile is given by Fig. 6 for the artery.

There are three possible breaking failures: (i) the circumferential break occurs first at $p < p_{\max}$; (ii) the longitudinal break occurs first at $p < p_{\max}$; (iii) both circumferential and longitudinal breaks occur at the pressure $p_{\max}$. From the design point of view, the third scenario is the best in that the tube wall has balanced (optimal) strengths in both directions.

3. Results

3.1. *Material properties*

The material parameters for examples of elastic tube A, B and C are shown in Fig. 5, with a comparison of the measured and estimated circumferential and longitudinal Cauchy stress components against the corresponding stretch ratios. The error in the stress components is estimated to be

$$\alpha = \frac{\sqrt{\sum_{i=1}^{N_L}(\sigma_{L_i} - \sigma_{L_i}^{\exp})^2 + \sum_{j=1}^{N_C}(\sigma_{C_j} - \sigma_{C_j}^{\exp})^2}}{\sum_{i=1}^{N_L}\sigma_{L_i}^{\exp} + \sum_{j=1}^{N_C}\sigma_{C_j}^{\exp}}. \tag{14}$$

Figure 5 shows that for the three tubes studied the fibre angle, β, (the angle between the fibre orientation and the circumferential direction) is in the range of 51.9°–55.2°, and the fibre stiffness, k_1, ranges from 19–24 MPa. The matrix material stiffness, μ, shows a variation of 2.5–3.7 MP. The fibre anisotropic property index, ρ, is 1.

The estimated parameters are compared with the microscopic observations shown in Fig. 3. The estimated fibre angle agrees very well with the microscopic observations, but is slightly larger ($\sim$2°). This is presumably because the fibres in these thin tubes present some degree of dispersion which is not taken into account.

These parameters are compared with human common carotid artery intact wall presented by Sommer [2008] in Table 2. To check the sensitivity of these parameters, we also provide the range of their variations based on a 10% error bar of the experimental data. It is clear the stiffness for the matrix material and fibres of the intact human artery wall are much lower than for the artificially made elastic tubes. Further, the fibre angle of the intact wall is less than half of the fibre angles of the elastic tubes. The fibre anisotropic property index is 0.8 in the artery, hence the artery tissue shows more significant dispersion in the fibre structure compared with the artificial tubes.

In the artificial tubes the fibre angle is normally greater than 45°; the fibres are more aligned in the longitudinal direction. In other words, the tube wall is stiffer longitudinally (see Fig. 5). For the intact human common carotid artery wall, however, the fibre angle is much less than 45°, and thus the artery is stiffer circumferentially (Fig. 6). The fibres in the human arteries also behave like continuous bundles [Smiley-Jewell *et al.*, 2002; Gasser *et al.*, 2006].

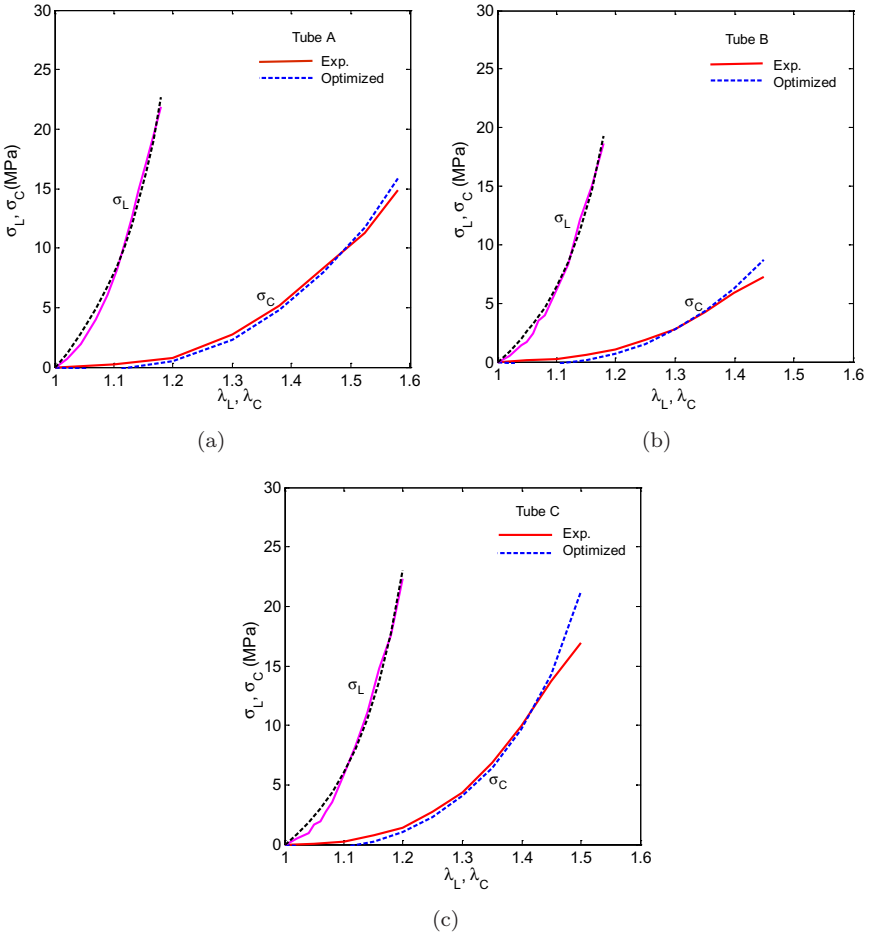

Fig. 5. Identified material parameters of fibres and matrix, and the comparison of measured and estimated Cauchy stress components for elastic tube A, B and C.

3.2. *Strains*

The elastic tube models of thickness 0.0203 mm and the intact common carotid artery of thickness 1.17 mm are then modeled using the FE package, ABAQUS. We use the membrane model (M3D4R) for Tube A, B and C, and the 3D solid model (C3D8H) for the common carotid artery [Sommer, 2008]. Again $p_{\max} = 1.5$ MPa is used for Tube A, B and C, the loading profile is the same as shown in Table 2. The measured breaking axial strain are $\varepsilon_L^b = 0.201, 0.183, 0.204$, for Tube A, B and C, respectively.

The internal pressure–time relation of the common carotid artery is determined according to the pressure–axial strain curve measured when the pressure is varied in 0–33 kPa (0–250 mmHg) [Sommer, 2008]. There is no data available on the breaking strain for the artery.

Table 1. The pressure loading profile.

Tube		Profile										
A	p (MPa)	0.000	0.084	0.194	0.327	0.477	0.641	0.813	0.990	1.167	1.340	1.500
	ε_L	0.000	0.020	0.040	0.060	0.080	0.101	0.121	0.141	0.161	0.181	0.201
B	p (MPa)	0.000	0.042	0.086	0.139	0.210	0.308	0.441	0.618	0.848	1.139	1.500
	ε_L	0.000	0.018	0.037	0.055	0.073	0.092	0.110	0.128	0.147	0.165	0.183
C	p (MPa)	0.000	0.015	0.045	0.093	0.167	0.271	0.417	0.607	0.845	1.138	1.500
	ε_L	0.000	0.020	0.041	0.061	0.082	0.102	0.123	0.143	0.163	0.184	0.204
Artery [Sommer, 2008]	p (kPa)	0.000	0.715	1.430	2.146	2.976	3.920	4.864	6.912	9.146	14.440	33.300
	ε_L	0.000	0.012	0.024	0.036	0.048	0.060	0.071	0.084	0.095	0.107	0.119

Table 2. Material parameters of the elastic tubes and human artery.

Constants	Tube A	Tube B	Tube C	Human common carotid artery intact wall [Sommer, 2008]
μ (MPa)	3.557	2.907	2.52	0.0445
	(3.424, 3.777)	(2.77, 3.055)	(2.346, 2.649)	
β (°)	55.476	53.9425	51.9014	20.4
	(54.923, 56.231)	(53.403, 54.527)	(51.465, 52.338)	
k_1 (MPa)	20.599	19.1658	24.0963	0.0284
	(18.711, 22.018)	(17.37, 20.63)	(22.263, 26.045)	
k_2	12.1404	16.907	18.0746	68.9
	(9.369, 14.557)	(14.5, 18.96)	(15.991, 19.71)	
ρ	1.0	1.0	1.0	0.8
	(1.0, 1.0)	(1.0, 1.0)	(1.0, 1.0)	
α	0.059	0.084	0.077	N/A
	(0.053, 0.062)	(0.075, 0.09)	(0.07, 0.084)	

Data in ( ) show the range of the variations if there are ±10% errors in the experimental data.

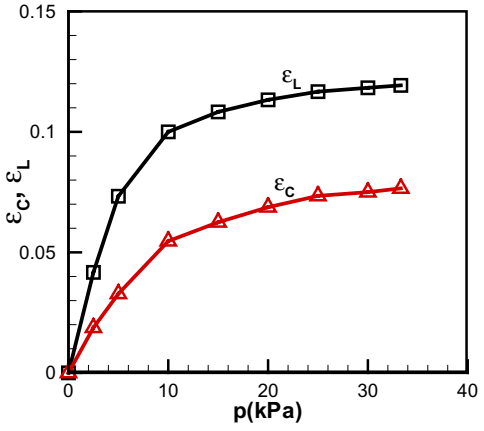

Fig. 6. Experimental circumferential and longitudinal strains of the human artery plotted against internal pressure [Sommer, 2008], showing the circumferential strain is less than half of the longitudinal strain.

The results are shown in Fig. 7, where the circumferential and longitudinal strains are plotted against internal pressure, and are compared to that of the common carotid artery. The experimental breaking criteria, $\varepsilon_c^b, \varepsilon_L^b$, are also marked in the figure. Figure 7 shows that the tube models have markedly different behavior compared to the human carotid artery. In all the tubes, the circumferential strain increases rapidly with the internal pressure initially, and then reaches a plateau. In fact, the maximum circumferential strain occurs at very low pressure (around 0.2–0.4 MPa). This significant observation suggests that if this maximum value reaches the breaking limit, the circumferential breaking will occur first. Indeed, for Tube A, which has a fibre angle of 55°, the maximum circumferential strain is over the breaking limit, so this tube will fail at much lower pressure. When the fibre angle

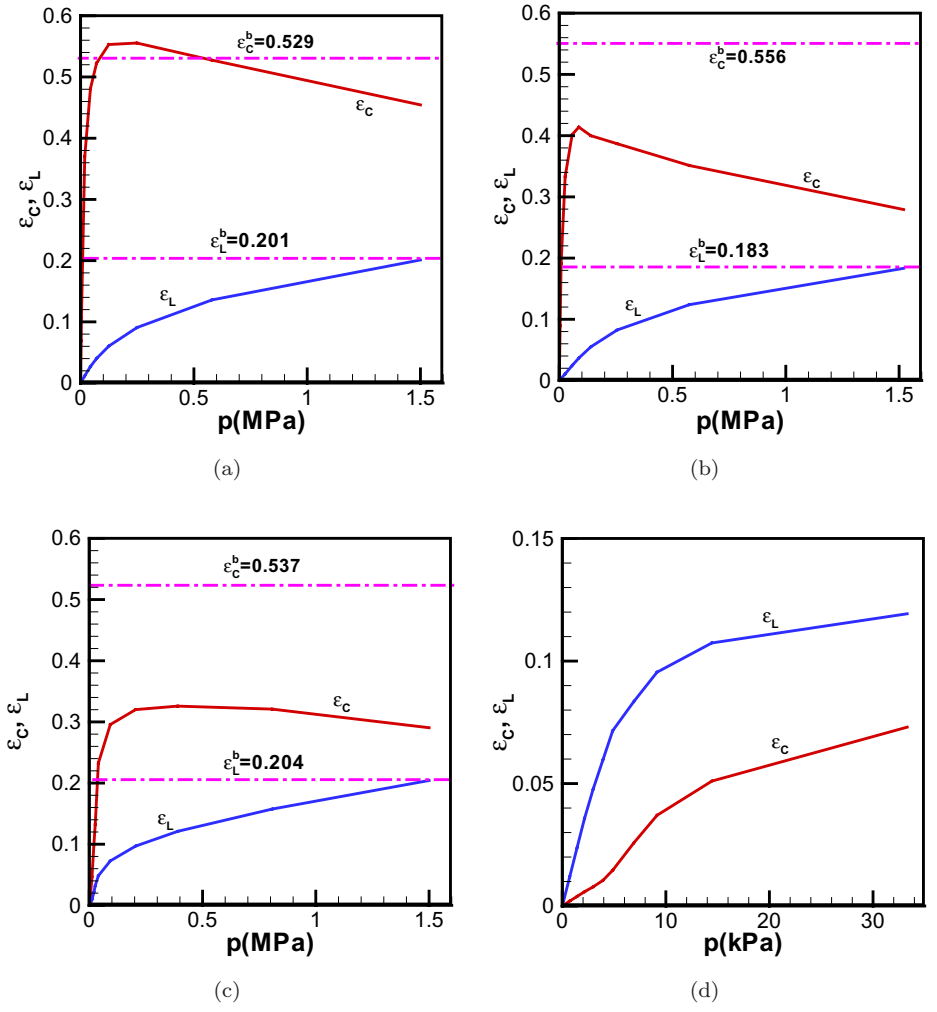

Fig. 7. The longitudinal and circumferential strains against pressure for (a) Tube A, (b) Tube B, (c) Tube C, and (d) human common carotid artery. The measured breaking strains, ε_c^b and ε_L^b, are indicated by the dot–dashed lines.

decreases, i.e., for Tube C, the peak circumferential strain is well below the breaking limit. These results indicate the current weakness of the tube design, and suggest that it is possible to vary the fibre angle to improve the tube performance.

We note that the common carotid artery has smaller fibre angle of around 20° compared with the tubes. Subsequently, both the circumferential and longitudinal strains reach their maxima at the highest pressure. If we adopt the strain limit proposed by Duenwald-Kuehl *et al.* [2012], then the artery may fail (if it fails at all) at the circumferential and longitudinal directions simultaneously.

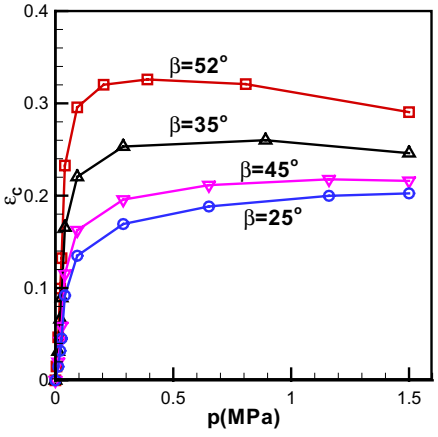

Fig. 8. The circumferential strain plotted against pressure for Tube C at various fibre angles, showing that the location of the maximum circumferential strain is shifted to the right when the fibre angle is decreased.

3.3. *Optimization of the fibre angle*

To clarify the effects of fibre angle on the tube deformation, we investigate the effect of changing the fibre angle in Tube C, while keeping the other mechanical conditions unchanged. The peak circumferential strains for fibre angles of 45°, 35° and 25° are plotted in Fig. 8. It is clear that the distribution of the circumferential strain is significantly affected by the fibre angle. The position of the maximum circumferential strain is closer to that of the maximum longitudinal strain or the maximum internal pressure when the fibre angle is $\beta = 25°$. Interestingly, this angle is close to the fibre angle of human common carotid artery ($\beta = 20.4°$). This suggests that the fibre angle of human common carotid artery is optimized by natural evolution.

4. Discussion

In this work, we developed a fibre reinforced model for artificial elastic tubes, and estimated the material parameters of the matrix and two families of fibres from experimental data obtained in two uniaxial tensile tests, assuming that transversal stress has no contributions in the tests. This assumption is in line with the standard uniaxial tensile test in mechanics of materials [Beer and Johnston, 1981].

The estimated fibre angles from the tensile tests agree excellently with the microscopic observations, with a small discrepancy of 2°–6°. The reason for this discrepancy may be that the fibres are nonuniformly distributed, as suggested by Fig. 3, which has not been accounted for in our models.

The polymer materials are typically subject to different failure modes: these are (i) breaking due to a steady loading in a uniaxial tensile test, (ii) fracture due to crack or crack-like defect growth in a material body at a constant loading, and

(iii) damage due a steady or cyclic loading [Powell, 1983]. For the thin artificial elastic tubes studied here, only the first failure mode is considered. We use the maximum strain/stretch as the breaking criterion and the breaking of the tubes is compared with the breaking behavior of the human carotid artery. The tubes are found to be at the risk of early circumferential breaking due to a local maximum of circumferential strain. The maximum position seems to be dependent on the fibre angles; the greater the fibre angle, the sooner the maximum occurs as pressure increases. Although there is no recorded data of the breaking limit for the human carotid artery walls, we found that the design of the carotid artery is superior to the artificial tubes, in that the circumferential stretch reaches the maximum at about the same time as the maximum longitudinal stretch when pressure is increased to its maximum.

It is worth mentioning that other failure modes may also be important for artificial tubes. A few damage models have been proposed for bio-tissue under cycling loading to account for the Mullins's or softening effect in stress–strain curves [Hokanson and Yazdani, 1997; Alastrué *et al.*, 2007; Volokh, 2008; Calvo *et al.*, 2009; Li and Robertson, 2009; Balzani *et al.*, 2009; Marini *et al.*, 2012; Martins *et al.*, 2012]. These different damage mechanisms have not been considered in this study.

5. Conclusion

Artificial thin-walled elastic tubes are modeled as a fibre reinforced membrane with two families of fibres imbedded in a homogenous matrix material. The mechanical properties and fibre angle of these tubes are inversely estimated using experimental data of tensile tests on the tube specimens taken in the circumferential and longitudinal directions. Our nonlinear inflation simulations show that the currently designed tube casings are not optimal under internal pressure and axial loading and could have premature break in the circumferential direction. In comparison, the human common carotid artery appears to have nearly optimal fibre structure in the sense that if failure occurs, it will occur in both the circumferential and longitudinal directions simultaneously. This work highlights the need for improved designs of the artificial thin-film elastic tubes.

Acknowledgment

This work is supported by an EPSRC Knowledge Transfer Award.

References

Alastrué, V., Rodriguez, J., Calvo, B. and Doblare, M. [2007] "Structural damage models for fibrous biological soft tissues," *International Journal of Solids and Structures* **44**(18), 5894–5911.

Balzani, D., Brinkhues, S. and Holzapfel, G. A. [2012] "Constitutive framework for the modeling of damage in collagenous soft tissues with application to arterial walls," *Computer Methods in Applied Mechanics and Engineering* **213–216**, 139–151.

Beer, F. and Johnston, E. [1981] *Mechanics of Materials* (McGraw-Hill International Company, Auckland).

Calvo, B., Pena, E., Martins, P., Mascarenhas, T., Doblaré, M., Natal Jorge, R. and Ferreira, A. [2009] "On modelling damage process in vaginal tissue," *Journal of Biomechanics* **42**(5), 642–651.

Chu, B. M., Frasher, W. G. and Wayland, H. [1972] "Hysteretic behavior of soft living animal tissue," *Annals of Biomedical Engineering* **1**(2), 182–203.

Diani, J., Fayolle, B. and Gilormini, P. [2009] "A review on the Mullins effect," *European Polymer Journal* **45**(3), 601–612.

Duenwald-Kuehl, S., Kondratko, J., Lakes, R. S. and Vanderby, R. [2012] "Damage mechanics of porcine flexor tendon: Mechanical evaluation and modeling," *Annals of Biomedical Engineering* **40**(8), 1612–1707.

Gasser, T. C., Ogden, R. W. and Holzapfel, G. A. [2006] "Hyperelastic modelling of arterial layers with distributed collagen fibre orientations," *Journal of the Royal Society Interface* **3**(6), 15–35.

Göktepe, S., Acharya, S., Wong, J. and Kuhl, E. [2011] "Computational modeling of passive myocardium," *International Journal for Numerical Methods in Biomedical Engineering* **27**(1), 1–12.

Hokanson, J. and Yazdani, S. [1997] "A constitutive model of the artery with damage," *Mechanics Research Communications* **24**(2), 151–159.

Holzapfel, G. A., Sommer, G., Gasser, C. T. and Regitnig, P. [2005a] "Determination of layer-specific mechanical properties of human coronary arteries with nonatherosclerotic intimal thickening and related constitutive modeling," *American Journal of Physiology-Heart and Circulatory Physiology* **289**(5), H2048–2058.

Holzapfel, G. A., Gasser, T. C. and Ogden, R. W. [2000] "A new constitutive framework for arterial wall mechanics and a comparative study of material models," *Journal of Elasticity* **61**(1), 1–48.

Holzapfel, G., Stadler, M. and Gasser, T. [2005b] "Changes in the mechanical environment of stenotic arteries during interaction with stents: Computational assessment of parametric stent designs," *Journal of Biomechanical Engineering* **127**(1), 168–180.

Li, D. and Robertson, A. M. [2009] "A structural multi-mechanism constitutive equation for cerebral arterial tissue," *International Journal of Solids and Structures* **46**(14–15), 2920–2928.

Marini, G., Maier, A., Reeps, C., Eckstein, H. H., Wall, W. A. and Gee, M. W. [2012] "A continuum description of the damage process in the arterial wall of abdominal aortic aneurysms," *International Journal for Numerical Methods in Biomedical Engineering* **28**, 87–99.

Marquardt, D. W. [1963] "An algorithm for least-squares estimation of nonlinear parameters," *Journal of the Society for Industrial & Applied Mathematics* **11**(2), 431–441.

Martins, P., Peña, E., Jorge, R., Santos, A., Santos, L., Mascarenhas, T. and Calvo, B. [2012] "Mechanical characterization and constitutive modelling of the damage process in rectus sheath," *Journal of the Mechanical Behavior of Biomedical Materials* **8**, 111–122.

Miehe, C. [1994] "Aspects of the formulation and finite element implementation of large strain isotropic elasticity," *International Journal for Numerical Methods in Engineering* **37**(12), 1981–2004.

Powell, P. [1983] *Engineering with Polymers* (Chapman and Hall, London).

Smiley-Jewell, S. M., Tran, M. U., Weir, A. J., Johnson, Z. A., Van Winkle, L. S. and Plopper, C. G. [2002] Three-dimensional mapping of smooth muscle in the distal conducting airways of mouse, rabbit, and monkey," *Journal of Applied Physiology* **93**(4), 1506–1514.

Sommer, G. [2008] *Mechanical Properties of Healthy and Diseased Human Arteries*, Institute of Biomechanics. Graz, Austria, Graz University of Technology.

Stevens, E. and Poliks, M. [2003] "Tensile strength measurements on bioploymer films," *Journal of Chemical Education* **80**(7), 810–812.

Volokh, K. [2008] "Prediction of arterial failure based on a microstructural bi-layer fibre–matrix model with softening," *Journal of Biomechanics* **41**(2), 447–453.

Wang, H. M., Gao, H., Luo, X. Y., Berry, C., Griffith, B. E., Ogden, R. W. and Wang, T. J. [2013] "Structure-based finite strain modelling of the human left ventricle in diastole," *International Journal for Numerical Methods in Biomedical Engineering* **29**(1), 83–103.